WILEY

RESEARCH ARTICLE

Stretchable, skin-conformable neuromorphic system for tactile sensory recognizing and encoding

Mengge Wu[1,2] | **Qiuna Zhuang**[3] | **Kuanming Yao**[2] | **Jian Li**[2,4] | **Guangyao Zhao**[2] | **Jingkun Zhou**[2,4] | **Dengfeng Li**[2,4] | **Rui Shi**[2] | **Guoqiang Xu**[2] | **Yingchun Li**[5] | **Zijian Zheng**[3] | **Zhihui Yang**[6] | **Junsheng Yu**[1] | **Xinge Yu**[2,4]

[1]State Key Laboratory of Electronic Thin Films and Integrated Devices, School of Optoelectronic Science and Engineering, University of Electronic Science and Technology of China (UESTC), Chengdu, the People's Republic of China

[2]Department of Biomedical Engineering, City University of Hong Kong, Hong Kong, the People's Republic of China

[3]Laboratory for Advanced Interfacial Materials and Devices, School of Fashion and Textiles, The Hong Kong Polytechnic University, Hong Kong, the People's Republic of China

[4]Hong Kong Center for Cerebra-Cardiovascular Health Engineering, Hong Kong Science Park, Hong Kong, the People's Republic of China

[5]College of Science, Harbin Institute of Technology, Shenzhen, the People's Republic of China

[6]Department of Pathology, The Affiliated Hospital of Southwest Medical University, Luzhou, the People's Republic of China

Correspondence

Xinge Yu, Department of Biomedical Engineering, City University of Hong Kong, Hong Kong, the People's Republic of China.
Email: xingeyu@cityu.edu.hk

Zijian Zheng, Laboratory for Advanced Interfacial Materials and Devices, School of Fashion and Textiles, The Hong Kong Polytechnic University, Hong Kong SAR, the People's Republic of China.
Email: tczzheng@polyu.edu.hk

Zhihui Yang, Department of Pathology, The Affiliated Hospital of Southwest Medical University, Luzhou 646000, Sichuan, the People's Republic of China.
Email: yzhih73@swmu.edu.cn

Junsheng Yu, State Key Laboratory of Electronic Thin Films and Integrated Devices, School of Optoelectronic Science and Engineering, University of Electronic Science and Technology of China (UESTC), Chengdu 610054, the People's Republic of China.
Email: jsyu@uestc.edu.cn

Abstract

Expanding wearable technologies to artificial tactile perception will be of significance for intelligent human–machine interface, as neuromorphic sensing devices are promising candidates due to their low energy consumption and highly effective operating properties. Skin-compatible and conformable features are required for the purpose of realizing wearable artificial tactile perception. Here, we report an intrinsically stretchable, skin-integrated neuromorphic system with triboelectric nanogenerators as tactile sensing and organic electrochemical transistors as information processing. The integrated system provides desired sensing, synaptic, and mechanical characteristics, such as sensitive response ($\sim$0.04 kPa^{-1}) to low-pressure, short- and long-term synaptic plasticity, great switching endurance ($>$10 000 pulses), symmetric weight update, together with high stretchability of 100% strain. With neural encoding, demonstrations are capable of recognizing, extracting, and encoding features of tactile information. This work provides a feasible approach to wearable, skin-conformable neuromorphic sensing system with great application prospects in intelligent robotics and replacement prosthetics.

KEYWORDS

neural encoding, neuromorphic sensing system, organic electrochemical transistors, tactile sensation, triboelectric nanogenerators

1 | INTRODUCTION

In biological somatosensory systems, the perception, transmission, and processing of information rely on the distributed parallel nervous networks to efficiently solve complex and unstructured real-world problems.[1,2] For instance, tactile sensation is associated with the conversion of mechanical signals to electrical signals by mechanoreceptors.[3] Then these electrical signals flow through nerve fibers to presynaptic membranes, inducing the release of neurotransmitters and firings of the postsynaptic membranes, and finally deliver them to the brain to form tactile sensations. Neural encoding and learning are performed in the processes of collaborating and handling external information. Inspired by biological systems, neuromorphic electronics have been developed to rebuild and enhance intelligent functions,[4] such as tactile perception,[5,6] artificial olfactory,[7,8] image recognition,[9,10] auditory communications,[11,12] and neuromorphic computing.[13,14]

Encouraged by the urgent need for intelligent robotics and replacement prosthetics, remarkable progress has been made in neuromorphic tactile systems with hierarchical structures for sensing and processing tactile information synergistically (Table S1).[15,16] Tactile sensors, which mimic mechanoreceptors, are constructed by resistive devices and triboelectric nanogenerators (TENGs).[17,18] Memristors and transistors are explored to mimic the biological synapses.[19–21] For instance, by integrating carbon nanotube-based pressure sensors with conjugated polymer-based transistors, the platform can sense objects' movements and recognize braille characters.[22] And activated by TENG, MoS_2 transistors consume energy as low as 11.9 fJ per spike, which is comparable with human synapses.[23] Recently emerging organic electrochemical transistors (OECT) exhibit outstanding performances compared with conventional transistors and show great promise for artificial synapse applications, such as more memory states, ease-to-flexibility, low energy consumption, and so on.[24,25] However, for such close-proximity integration with machine terminals, the neuromorphic system needs to be flexible, stretchable, skin-integrated, and conformable, so as to enable good wearability and reliable interconnection between soft and rigid components.

Here, we report a stretchable, skin-conformable neuromorphic tactile system consisting of TENG tactile sensors and hydrogel-gated OECT synapses. It provides desired pressure sensing, synaptic, and mechanical characteristics, including ultralow-sensitive detection with a linear sensitivity of $0.04\ kPa^{-1}$ in (0.24, 23.56 kPa), tremendous memory states, symmetric weight update, and excellent stretchability (∼100% strain). Our neuromorphic tactile system can sense, combine, and recognize/distinguish multiple pressure inputs, as confirmed by the demonstrations of the Morse Code Reader and handwritten alphabet-based human–machine interface.

2 | RESULTS AND DISCUSSION

2.1 | Characterization of stretchable tactile sensors

Inspired by the biological nervous systems, our neuromorphic systems are constructed with a similar
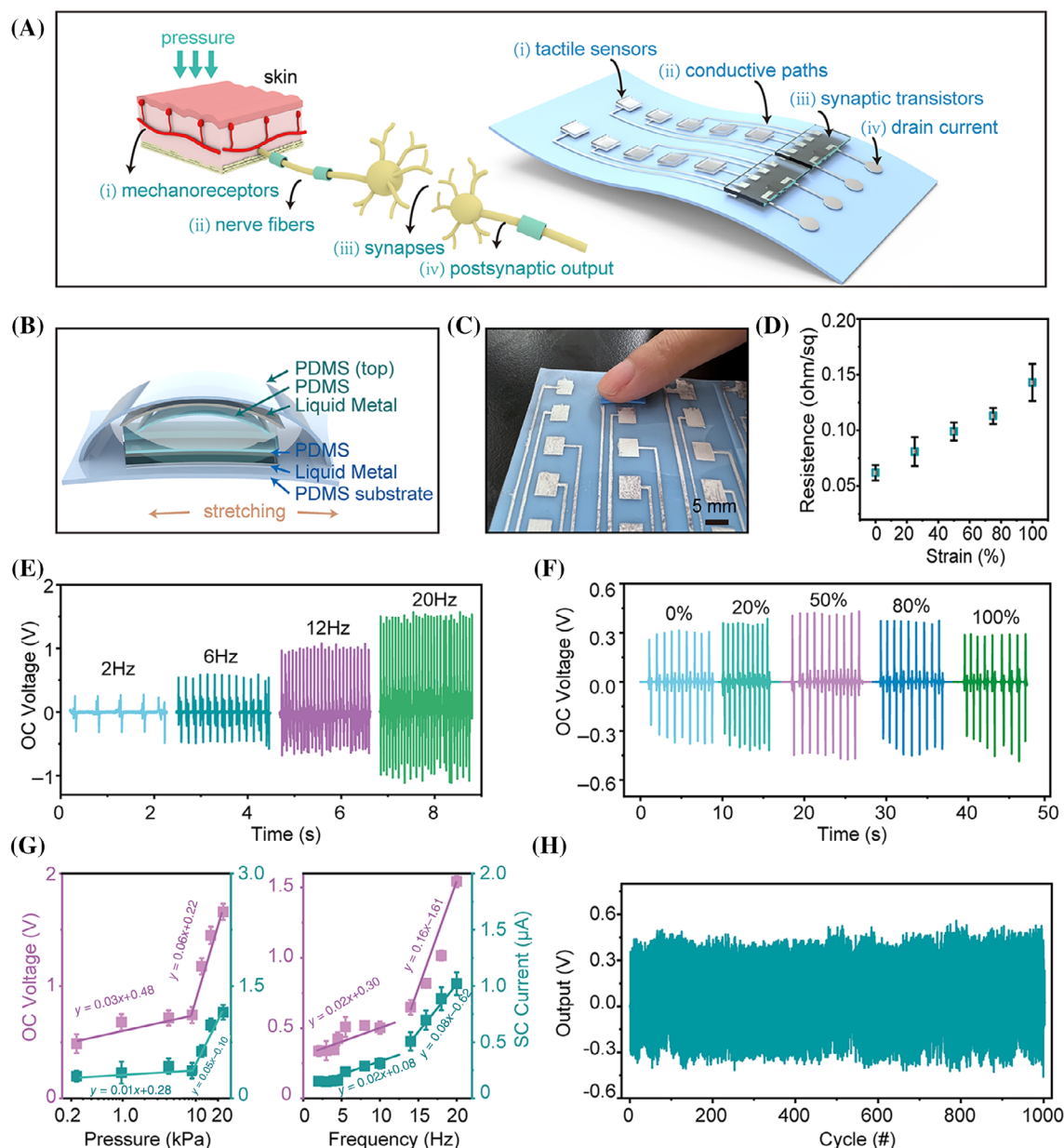
FIGURE 1 Performance characterization of stretchable TENG tactile sensors. (A) Schematic diagram of the biological and neuromorphic sensing and processing system. (B) Schematic of TENG configuration. (C) Optical image of volunteer tapping the TENG tactile sensor, simulating an external pressure applied on human skin. (D) Explore the relationship between sheet resistance of EGaIn electrode and strain. (E) OC voltages of TENG (under strain-free state) at frequencies of 2, 6, 12, and 20 Hz. (F) OC voltages of TENG are obtained from continuous strain motions, and the tensile properties of TENG outputs are non-directional. (G) Explore the relationship between output performance (OC voltage that is in purple, and SC current that is in green) and applied pressure (left image), and frequency (right image). (H) Stability and durability tests of stretchable TENG undergoing a continuous 1000 cycles within 600 s.

hierarchical structure (Figure 1A): (i) TENGs simulate the mechanoreceptors for pressure detection; (ii) conductive paths mimic nerve fibers for transmitting potentials; (iii) OECTs simulate synapses for processing the information; (iv) the drain current of OECTs simulates the postsynaptic output that will be transmitted to the brain. The fabrication process and demonstrated examples are illustrated in Figures S1 and S2. Polydimethylsiloxane (PDMS, 30:1, ~100 kPa[26]) is used as a stretchable substrate to

provide an adhesive interface with skin (Figure S3). PDMS films with curing ratios of 10:1 (~400 kPa) and 20:1 (~1500 kPa) serve as friction layers, and the liquid metal eutectic gallium–indium (EGaIn) acts as the electrodes due to its favorable conductivity and stretchability (Figure 1B).[27] Figures 1C and S4 show the pressure applied to TENG. As shown in Figure 1D, the resistance of EGaIn increases from 0.062 ± 0.007 to 0.143 ± 0.017 ohms sq^{-1} when stretched from 0% to 100%, suggesting excellent

stretchability and conductivity over traditional Au electrodes.[28] The working mechanism of this TENG is illustrated in Figure S5. Put simply, triboelectric electrons are generated when two PDMS friction layers contact due to their different frictional polarities. To maintain the charge balance, charges are induced in two EGaIn electrodes, and then alternating currents are formed. Repeated contact-separation behaviors convert mechanical information to electrical impulses. To provide a benchmark for tactile sensing, the TENGs are first investigated in a strain-free state, and open-circuit voltage (V_{OC}) and short-circuit current (I_{SC}) are shown in Figures 1E and S6. Experienced increasing frequency from 2 to 20 Hz at the pressure of ~8.90 kPa, V_{OC} and I_{SC} gain from 0.26 to 1.53 V, and 0.28 to 1.47 μA, respectively. Under continuous stretched motions, the V_{OC} and I_{SC} rise approximately from 0.31 to 0.44 V, and 0.52 to 0.78 μA, respectively (Figures 1F and S7). The increased trend (0%–50% strain) stems from the positive effect of the larger contact area.[29] Nevertheless, a slight output reduction is observed when further stretched to 100%, resulting from the negative effect of increased electrode resistance. The TENG tactile sensors are expected to be insensitive to tensile force and maintain great operation stability in various deformations. It turns out that such stretchability boosts the adaptability of our devices in harsh environments.[30]

In Figure 1G, as we experienced increasing pressure from 0.24 to 23.56 kPa (the general human pressure perception range[31]) at 1 Hz, V_{OC} gains from 0.448 ± 0.042 to 1.716 ± 0.145 V, and I_{SC} grows from 0.319 ± 0.029 to 1.137 ± 0.128 μA, respectively. Then the pressure sensitivity is calculated to be 0.037 kPa^{-1} in (0.24, 8.90 kPa) and 0.040 kPa^{-1} in (8.90, 23.56 kPa), revealing the reliable triboelectric responses. And the linearity values are calculated to be 3.39 and 6.64 VkPa^{-1} in (0.24, 8.90 kPa) and (8.90, 23.56 kPa), respectively, demonstrating the great linearity of this tactile sensor. Besides, the frequency response is studied. Experiencing frequencies from 0.5 to 20 Hz at a constant pressure of 8.90 kPa were conducted by a linear motor. The sensitive and fast response to low-frequency signals makes this stretchable TENG a promising candidate for fast adaptive stress transduction.[32] The V_{OC} was maintained at 0.45 V in 600 ongoing contact-separation cycles (Figure 1H), demonstrating excellent stability and durability that are essential for practical applications.

2.2 | Characterization of stretchable synapse transistors

Here, all-solid-state transistors are favorable for integrating them into advanced rigid electronics. Inspired by the biological synapse (Figure 2A), OECT was constructed to mimic the functions of memory and computing, where the gate simulated the presynaptic voltage (orange arrow), ions in the electrolyte simulated the neurotransmitters that can regulate the drain current (simulated the postsynaptic current, green arrow). Figure 2B exhibits the OECT configuration, where PEDOT:PSS serves as the active channel, and soft PAAMPSA is introduced to promote its stretchability. Besides, hydrogel electrolytes are designed with a balance of high water-content, low volatility, and high conductivity. Aqueous NaCl is used as the ionic conductor due to the high conductivity and sensitive response of PEDOT:PSS to Na$^+$.[33] Polyacrylamide is selected as the elastomeric network because of its high toughness. The electrolytes are synthesized by dissolving acrylamide monomer, polyacrylamide, crosslinker, and photoinitiator in aqueous NaCl, and more details on NaCl hydrogel can be found in the Experimental Section and Figure S8. The working principle of PEDOT:PSS-based OECT can be simply explained as follows: The ions in the electrolyte enter and exit the PEDOT:PSS channel, resulting in changes in the polarity of the PEDOT group, conductivity of the channel, as well as drain current.[34] And the polarity regulation of the PEDOT group by gate voltage is displayed in Figure S9. Figure 2C exhibits our transistors with stretchable and skin-compatible properties. In Figure 2D,E, the PEDOT:PSS/PAAMPSA yields a resistance of 1.1 ± 0.2 kohm cm^{-1}, a maximum strain of 110%, and a Young's modulus of 14.31 MPa in the strain-free state. No obvious change is found with 50% strain, while it rises to 4.0 ± 0.3 kohm cm^{-1} for 100% strain and is accompanied by cracks that would disrupt the transconductance. Such desirable stretchability originates from the reduced tensile modulus. PAAMPSA contains sulfate and amide groups, which allow the formation of a polymer network between PAAMPSA and PEDOT:PSS via ionic and hydrogen bonds (Figure S9). When applied strain, the dynamic ionic and hydrogen bonds between PEDOT, PSS, and PAAMPSA can easily break and reconnect to disperse mechanical stress, offering mixed film highly stretchability.[35] In Figure 2F, the hydrogel possesses a low Young's modulus of 31.73 kPa and can be stretched to a maximum deformation of 30%, which could be further promoted by improving its toughness.[36] And hydrogel resistance maintains at 5.6 ± 0.5 kohm cm^{-1} under consecutive strain (Figure 2G), proving a stable reservoir for signal transduction. Then the electrochemical performances are investigated to evaluate the weight of OECT synapses (Figure 2H). The upward trend in transconductance is observed in devices with 0.1, 0.5, and 1.0 M NaCl-based hydrogel, and the maximum values of 17.7 ± 1.0 mS are obtained from the 0.5 M group at drain voltage (V_d) of −0.4 V. It is because more cations in 0.5 M
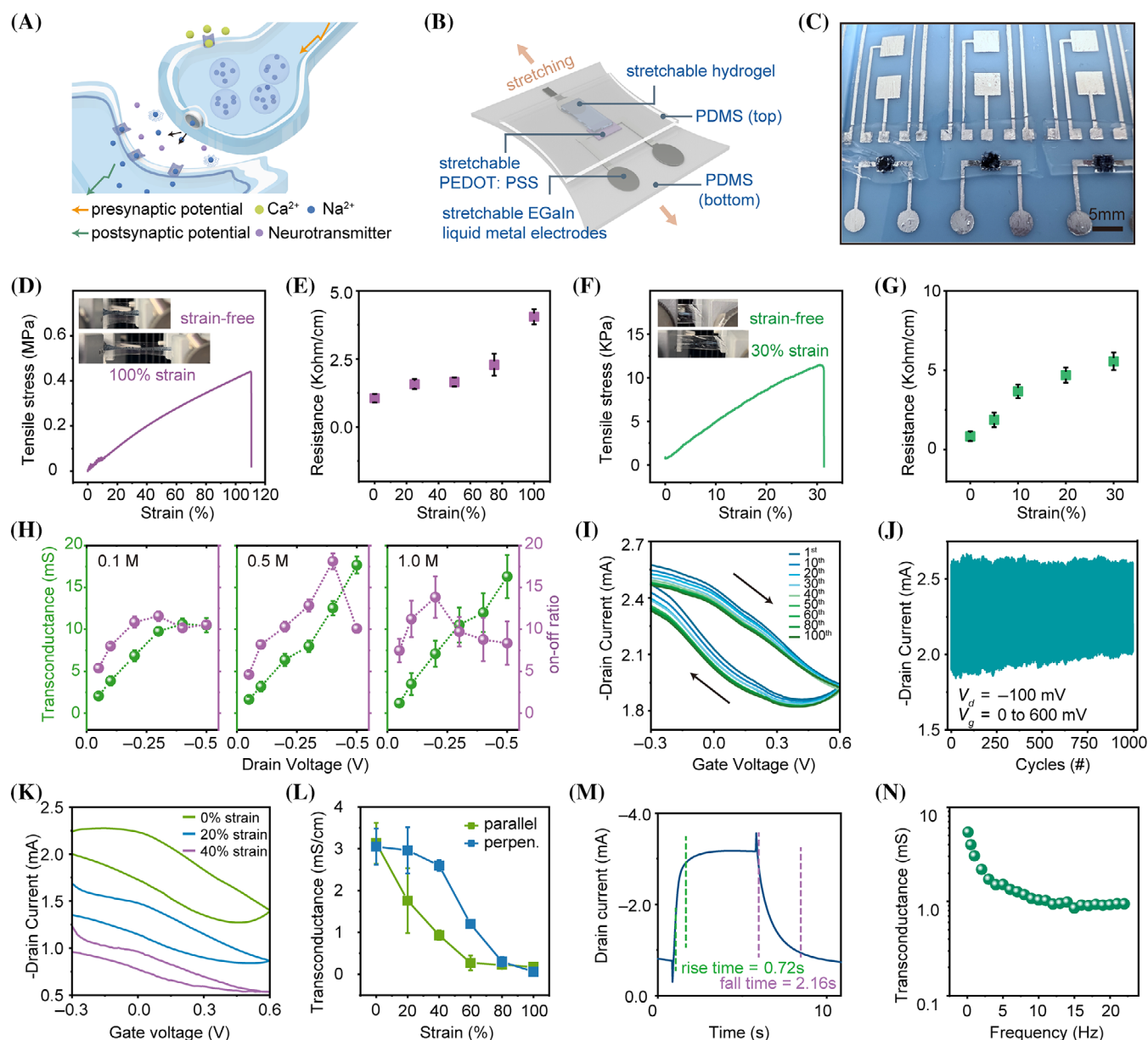
FIGURE 2 Performance characterization of stretchable OECT synapses. (A) Cartoon diagram of biological synapse, which transmit information via neurotransmitters. (B) Design of the stretchable OECT synapse. (C) Optical images of all-solid state OECT synapse. (D) Tensile stress–strain of the PEDOT: PSS film. (E) Normalized resistance of PEDOT: PSS as the function of strain. (F) Tensile stress–strain of the 0.5 M NaCl-based hydrogel. (G) Normalized resistance of 0.5 M NaCl-based hydrogel as the function of strain. (H) Transconductance and on–off ratio with 0.1, 0.5, and 1.0 M NaCl-based hydrogel as the electrolytes in OECT, respectively. (I) Hysteresis loops during 100 times of bidirectional scans. (J) Operational stability of this all solid-state OECT for 1000 cycles of gate voltage pulsing between 0 and 600 mV, at drain voltage of -100 mV. (K) Hysteresis loops with 0%, 20%, and 40% parallel strain. (L) Normalized transconductance of OECT at various strains, demonstrating a slower decay rate for stretched along perpendicular to the channel length direction than along parallel direction. (M) Rise time and fall time of OECT with 0.5 M NaCl-based hydrogel as electrolyte. (N) The relationship between transconductance and gate frequency (0.1, 22 Hz).

flow into the channel and participate in the doping/de-doping processes. However, the on–off ratio decreases at higher V_d, due to both on- and off-state currents increasing with V_d. Overall, the 0.5 M NaCl-hydrogel is the optimized one for the subsequent experiments. Furthermore, histograms of V_{oc} and transconductance values were

conducted in Figure S10, demonstrating that unit devices proposed in this work present great device uniformity.

The hysteresis of transfer curves under forward/reverse scans is correlated with their memory behaviors.[37] Typically, with greater hysteresis comes a better memory effect.[34] Hysteresis is associated with the time

constant of the migration of cations from the electrolyte to the active channel.[38] The maximum hysteresis window (MHW) is utilized to evaluate the hysteresis degree and is defined as the maximum difference value of the gate at the same drain current in the hysteresis loop. Figure S11 and Table S2 explores the relationship between MHW and V_d, where V_g was controlled over a typical range (−0.3 V, 0.6 V) with bidirectional scanning. A maximum MHW value of 0.42 ± 0.02 V is achieved when V_d is −0.1 V. A decrease in MHW values with V_d decreasing from −0.1 to −0.5 V, results from the suppressed doping/dedoping of the channel at higher V_d (absolute values).[39] Generally, the hysteresis also induces variations of threshold voltage in forward and reverse scans (Figure S12). Taking the memory effect and energy consumption into account, V_d is biased at a constant −0.1 V in the following synaptic plasticity measurements.

The hysteresis loops with 100 bidirectional scan cycles (Figure 2I) and great operational stability measured at 1000 consecutive pulses (Figure 2J) offer a solid foundation for practical applications. Further stability improvements can be achieved via material synthesis, optimizing device, structure and the operation conditions.[40,41] OECT yields a normalized transconductance (G_m) of 3.13 ± 0.49 mS cm^{-1} in the stain-free state (Figure 2K,L). Then G_m drops by 70% and 14% when devices are stretched to 40% in parallel and perpendicular to the channel-length direction, respectively. Further stretching to 100% will cause G_m to decay significantly, and this decay results from the negative changes in carrier mobility.[42] Optimization strategies in materials engineering and honeycomb porous structures have been conducted to improve tensile stability.[25,43] Response time and frequency response of the OECT synapse are investigated in Figure 2M,N. A larger rise/fall time of ∼0.72 and 2.16 s is obtained. It is far slower than that in liquid electrolyte OECT (in ms),[44,45] but it can amplify the rapid spikes of TENG from 100 ms to several seconds of excitatory/inhibitory postsynaptic currents. This property enables the recognition of handwritten information. However, the slow speed limits the frequency response to <22 Hz (Figure S13). An obvious decay in transconductance is found with frequency increasing in Figure 2N. It falls from 5.42 ± 0.05, to 1.04 ± 0.04, then to 0.94 ± 0.03 mS when the frequency increases from 0.1, to 10 and 22 Hz. To promote response speed, advanced material design is required to offer desirable carrier mobility.[46]

2.3 | Characterization of advanced synaptic functions

Synaptic plasticity, including excitatory/inhibitory postsynaptic currents, paired-pulse facilitation/depression, and short- and long-term potentiation/depression, is emulated to validate the feasibility of OECT synapses.[37] Synaptic depression is related to sensory adaptation, which is regarded as an efficient method for tracking and encoding rapid information updates.[47] In Figure 3A, a typical inhibitory postsynaptic current depression was triggered by 50 mV V_g with a 50 ms duration time (t_{dur}). At the moment of the gate pulse being applied, the capacitors in OECT are positively or negatively charged, which are named polarization and depolarization, respectively (Figure S14).[48] The inhibitory postsynaptic current decays back to resting current in approximately 4 s after removing the V_g. Then paired consecutive pulses with 50 mV peak amplitudes, a t_{dur} of 50 ms, and an interval time (t_{int}) of 30 ms are applied, yielding a typical paired-pulse depression result. Then the spike-number-dependent inhibitory postsynaptic current is investigated. The inhibitory postsynaptic current peaks (A_n, triggered by pulses with 200 mV) increase from 40.4 ± 3.7, to 125.0 ± 11.4, then to 173.9 ± 18.1 μA for pulse numbers increasing from 10, 50, and 100. The similar results obtained from pulses with 400 and 600 mV, further verify the synaptic depression (Figure S15). The energy consumption is 6.15 μJ for such a depression behavior in Figure 3A, and a detailed calculation is displayed in the Experimental Section. Figure 3B shows the pulse-duration-time dependence of the inhibitory postsynaptic current charge ratio, which is defined as $(A - A_0)/A_0 \times 100\%$, where A and A_0 are the active and resting currents, respectively. The charge rate of inhibitory postsynaptic current increases with t_{dur} both in volatile (change with t_{dur}) and non-volatile (maintains a stable level, not relevant to t_{dur}) regimes, suggesting the feasibility of bio-controlling short- and long-term plasticity.[48] Furthermore, single, paired, and multiple pulses with an amplitude of −50 mV, a t_{dur} of 50 ms, and a t_{int} of 30 ms are applied to explore facilitation behaviors (Figure 3C). The energy consumption is estimated to be 5.8 μJ per spike for such facilitation behavior. Detailed spike-height-dependent inhibitory/excitatory postsynaptic currents are summarized in Figure S16. Positive correlations are observed with linearities of 408 and 102 μA V^{-1} for depression and facilitation behaviors, respectively. Besides, spike-duration-time-dependent postsynaptic currents are analyzed in Figure S17, and great linearities of 1.52 and 1.34 μA ms^{-1} are obtained in depression and facilitation behaviors, respectively. As a supplement, the spike-number-dependent excitatory postsynaptic currents in facilitation mode are displayed in Figure S18, where pulses with a potential of −500 mV, a t_{dur} of 50 ms, and a t_{int} of 30 ms are applied. It turns out that with greater pulse numbers come larger excitatory postsynaptic current peaks. For instance, A_5 of 269.5 ± 11.4 μA, A_{50} of 366.3
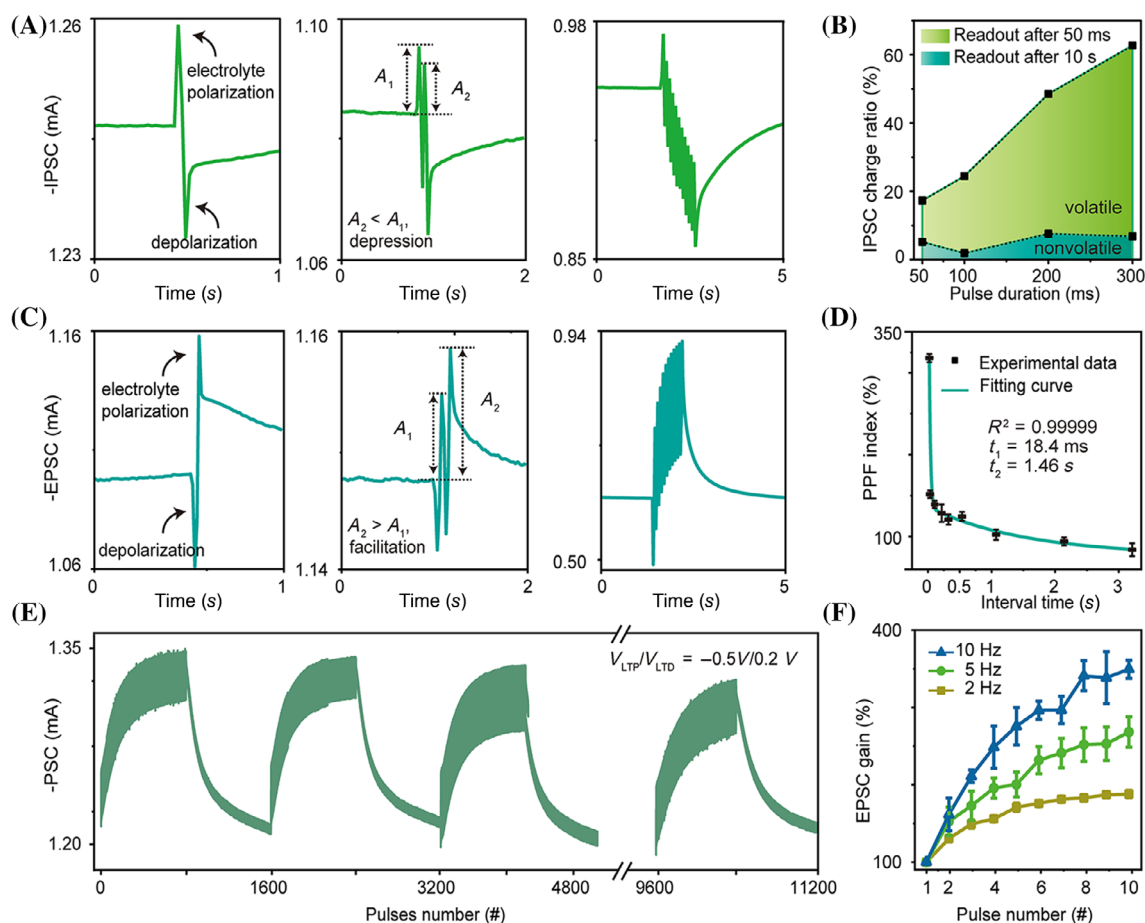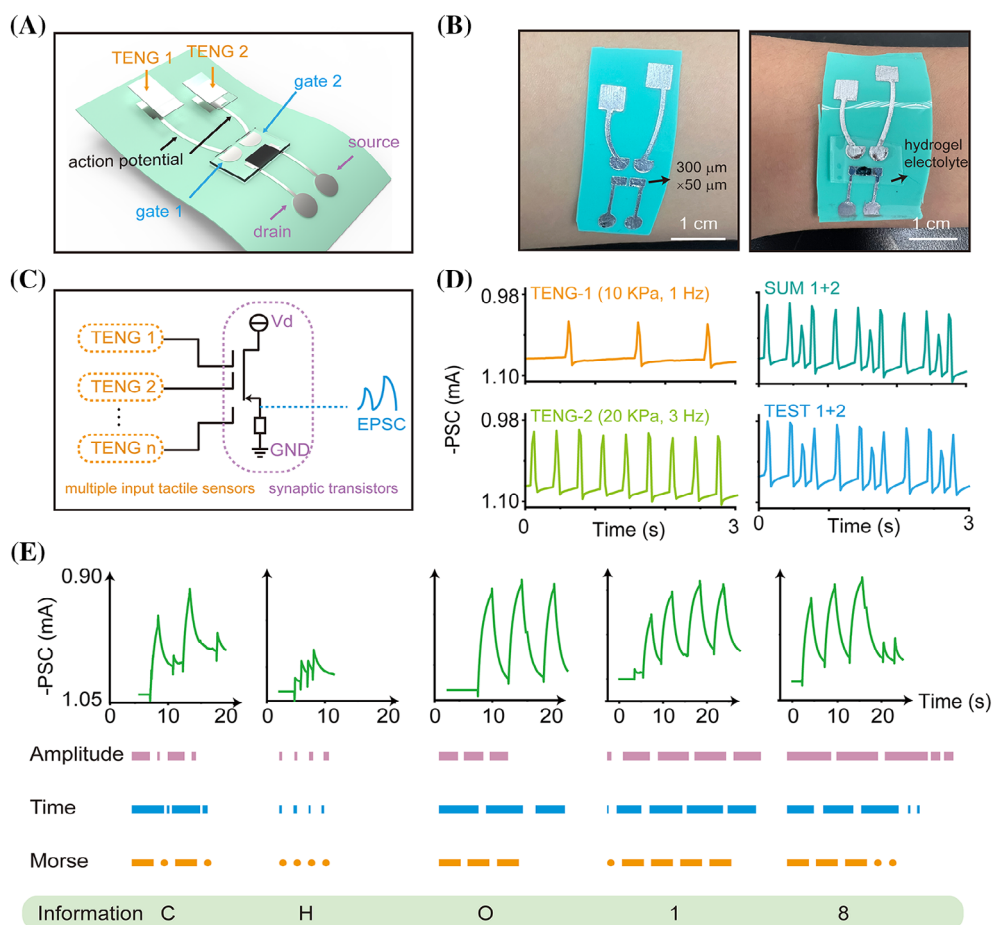
FIGURE 3 Characterizing the basic synaptic plasticity of OECT synapses. (A) Characterization of depression behaviors of single pulse (50 mV, duration time of 50 ms), paired pulses (50 mV, duration time of 50 ms, and interval time of 30 ms), and 10 pulses (200 mV, duration time of 50 ms, and interval time of 30 ms). (B) Pulse duration time dependence of the IPSC charge ratio when triggered by single pulse with amplitude of 50 mV. (C) Characterization of facilitation behaviors of single pulse (-50 mV, duration time of 30 ms), paired pulses (-50 mV, duration time of 50 ms, interval time of 30 ms), and 10 pulses (-200 mV, duration time of 50 ms, and interval time of 30 ms). (D) The plot of PPF index as the function of interval time. (E) Investigation of long-term potentiation-depression cycles, with 1600 pulses per cycle. (F) Evaluating dynamic filtering behavior by triggering with 50 mV at 2, 5, and 10 Hz.

$\pm$ 20.8 µA, and A_{200} of 465.1 $\pm$ 25.2 µA are achieved. The paired-pulse facilitation index (expressed as $A_2/A_1 \times 100\%$), indicating the facilitation quality, is plotted in Figure 3D. The maximum paired-pulse facilitation index is 318% $\pm$ 5% at a t_{int} of 20 ms, then it returns to 100% with t_{int} increasing. A paired-pulse facilitation curve can be described by a biexponential function of $y_1\exp(-\Delta t_{int}/\tau_1) + y_2\exp(-\Delta t_{int}/\tau_2) + y_0$, where y_1 and y_2 are the facilitation magnitudes of two decay phases, which are estimated to be 530.0% and 59.3%, respectively. τ_1 and τ_2 refer to the response times and are estimated to be 18.4 ms and 1.46 s. y_0 represents the fixed offset, which is estimated to be 76.7%. Besides t_{int}, spike amplitude also affects paired-pulse facilitation/depression behaviors. Figure S19 explores the spike-height-dependent excitatory postsynaptic currents for paired-pulse facilitation. Notably, a maximum paired-pulse facilitation index of 190.3% is obtained

at -0.4 V. The inverted "U" trends result from the trade-off between efficient polarization for A_1 and inefficient depolarization before A_2.

In the long-term potentiation-depression cycles (LTP-LTD), optimized V_{LTP} of -0.5 V and V_{LTD} of 0.2 V are applied, giving a dynamic range of 800 (Figure 3E). Exactly 11 200 pulses are conducted to examine the switching endurance, and an ignorable degradation is achieved. Higher linearity and symmetricity are obtained at lower pulses/cycles of 200, 400, and 600 (Figure S20), owing to the adaptation of the polarization response.[48] Besides, the dynamic filtering behaviors are evaluated by the excitatory postsynaptic current gains (A_n/A_1). In Figure 3F, pulses with a 50-mV potential and frequencies of 2, 5, and 10 Hz are applied. It turns out that with higher frequency come greater excitatory postsynaptic current gains. And similarly,

FIGURE 4 Characterizing the encoding strategies of bioinspired neuromorphic system. (A) Schematic illustration of integration system where synaptic transistor activated by two TENG tactile sensors. (B) Optical images of integration neuromorphic tactile system with two TENG input. (C) Circuit diagram of synaptic transistor activated by multiple tactile inputs. (D) EPSC signals obtained from TENG tactile sensors. (E) Demonstration of the Morse Code reader.

with more pulses come greater excitatory postsynaptic current gains. The above results indicate our transistors can well mimic basic synaptic functions.

2.4 | Encoding and learning handwritten alphabets

A single transistor synapse that integrates multiple tactile inputs is illustrated in Figure 4A–C. To explore the working principle of this system, the transistor is activated by pressures on TENG-1 (10 kPa, 1 Hz) and TENG-2 (20 kPa, 3 Hz). Figure 4D displays the postsynaptic current results obtained from individual TENG-1 (first panel), individual TENG-2 (second panel), the sum of the first and second panels (third panel), and the simultaneous application of TENG-1 and TENG-2 (fourth panel). Comparable results both in time and frequency domains, suggest that the fourth panel comprises two pressures of (10 kPa, 1 Hz) and (20 kPa,

3 Hz) by linear overlay. Such an ability to distinguish and integrate the simultaneous pressure inputs well rebuilds the function of biological synapses.

Using the encoding information function, we demonstrate a Morse Code reader. As shown in Figure S21, the contact motions yielded positive presynaptic currents and then induced postsynaptic currents to decrease (absolute values). Conversely, the separation motions yielded negative presynaptic currents and then induced postsynaptic currents to increase (absolute values). Tactile information can be encoded in the amplitude and time of active potentials related to touch motions. Encoded amplitude is the change in PSC, and encoded time is the time consumed during the PSC rise process. More detailed encoding strategies can be found in Figure S22. It turns out that shorter-time touches (dots in Morse Code) induce low-amplitude postsynaptic current signals with shorter potential times, whereas longer-time touches (dashes in Morse Code) induce large-amplitude postsynaptic current signals with longer
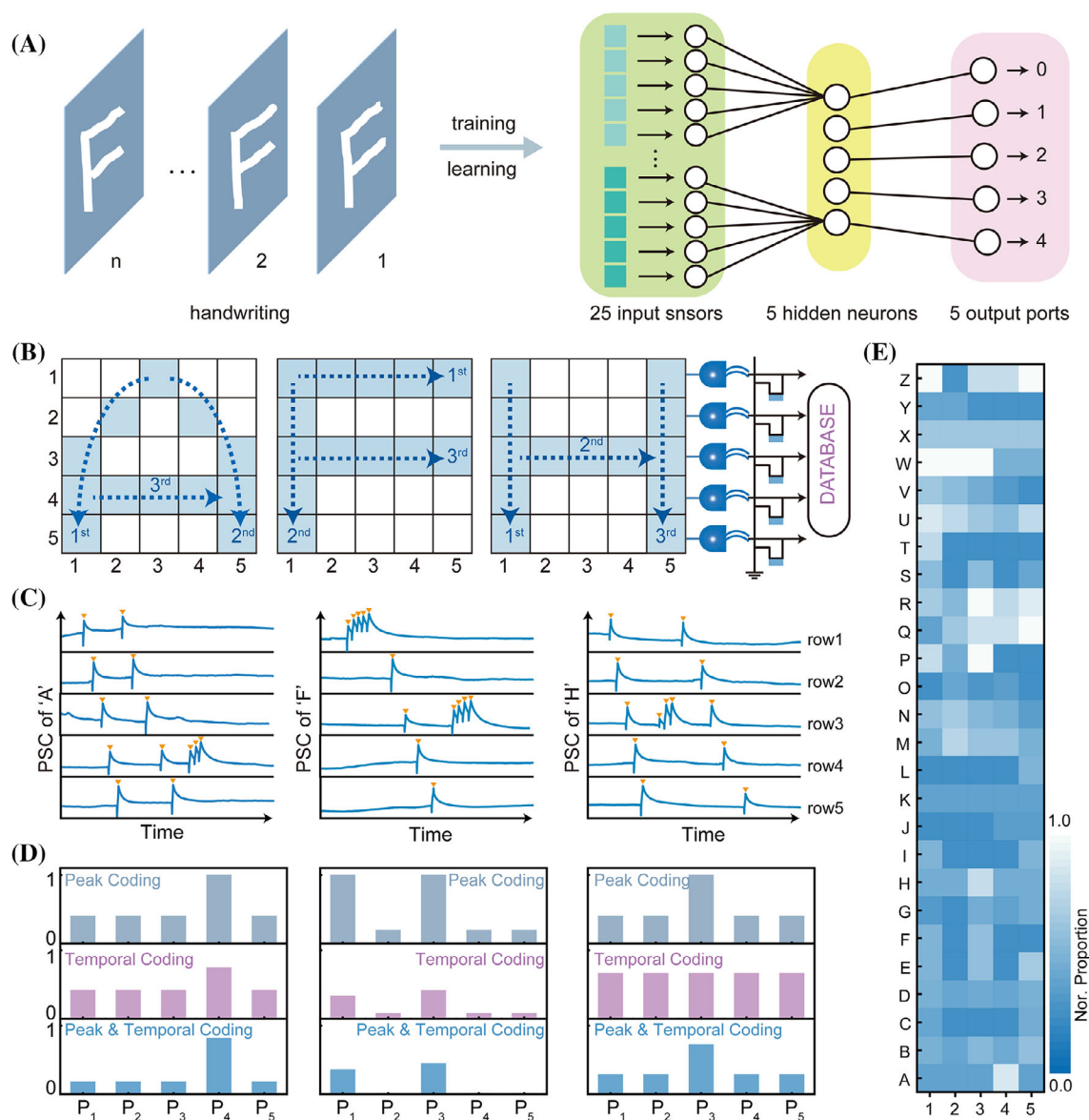
FIGURE 5 Demonstration of handwritten information-based human-machine interface. (A) Schematic diagram of handwriting recognition using integration neuromorphic system. (B) Structure and working mechanism of the integration neuromorphic system, and the demonstration of the writing paths for letters "A", "F", and "H". (C) Five-dimensional EPSC signals obtained from handwritten "A", "F", and "H" in the TENG tactile array. (D) Encoding 5-dimensional EPSC signals of "A", "F", and "H" in the forms of peak-feature extraction (gray columns), Temporal encoding (purple columns), and peak-timing-convolution encoding (blue columns). (E) Directory of alphabet encoding with peak-feature and temporal information.

potential times. Therefore, typical letters and numbers such as "C", "H", "O", "1", and "8" can be correctly recognized (Figure 4E) via two encoding strategies. And the postsynaptic current signals responding to tactile information from Morse Code are summarized in Figures S23 (alphabet) and S24 (numbers). To evaluate the noise level of this system, the jitters in postsynaptic current curves are regarded as noise. And the minimum signal-to-noise (SNR) ratio is calculated to be 19.45 dB. Besides, the flow charts of the training process are displayed in Figures S25–S27.

Furthermore, utilizing the function of handling multiple inputs, we demonstrate a handwritten information-based human–machine interface. To simplify the information processing, a reduced-dimensionality structure is introduced for extracting and encoding the tactile information. In such a design, 5×5 TENG sensors act as tactile input, and 5 synapse transistors serve as hidden neurons to process information (Figure 5A). Instead of extracting 25-dimensional information from the TENG array, such designs extract 5-dimensional (5D) postsynaptic current signals from OECTs. Once touches occur on tactile

sensors in any row, postsynaptic current signals are generated on the corresponding transistor. For instance, letters "A", "F", and "H" written in the paths (Figure 5B) yield the corresponding 5D postsynaptic current signals (Figure 5C). And a maximum SNR of 41.2 dB was obtained, demonstrating the great tactile sensitivity of this system. These orange triangles mark the active peaks induced by handwriting, which are captured easily via the "find-peaks" command in MATLAB. Three encoding strategies, including peak (gray columns), timing (purple columns), and peak-timing-convolution (blue columns), are applied to recognize the tactile information (Figure 5D). For peak-feature extraction, the proportion is defined as the peak number in each row, and they are (2, 5), (1, 5), and (2, 5) for "A", "F", and "H", respectively. For the temporal-feature encoding, proportion is defined as the time differences between the last and the first handwritten entries in each row. To improve the inclusiveness of writing strokes and speed, each touch is assigned 1 s. Then it is (5, 9), (1, 4, 5), and (8) for "A," "F," and "H," respectively. Due to the need to record time information and row positions when marking peaks, then perform integer assignment and subtraction operations on the time vector, temporal feature extraction requires three times as much computation as peak number extraction. More information on the temporal extraction process can be found in Figure S28 and note. However, writing the alphabet produces a small amount of data for the 5D PSC, and both methods can finish the operation within 1 min and obtain 100% accuracy. Since it involves more information, the peak-timing-convolution encoding strategy owns higher accuracy and precision. And they are calculated to be (10, 45), (1, 20, 25), and (16, 40) for "A", "F", and "H", respectively. Due to the different writing path, the obtained codes are completely different and can be used to distinguish the tactile information, revealing the feasibility of this encoding method. Writing paths for the alphabet are shown in Figure S28. Therefore, the alphabet directories of codes are formed using peak-timing-convolution encoding (Figure 5E) and other two strategies (Figure S29), which can be used as references and feature learning of handwritten inputs.

3 | CONCLUSIONS

Inspired by biological neural networks, we exploit an integration strategy for stretchable, skin-conformable neuromorphic systems to recognize and encode tactile sensory information. Stretchable functional materials lay a solid foundation for incorporating neuromorphic computing-based systems into wearable smart electronics with the features of skin-compatibility and skin-conformability. Benefiting from hierarchical structures of TENG sensors and OECT synapses, our neuromorphic systems are capable of recognizing Morse code and handwritten letters. As demonstrations, a parallel network consisting of 5×5 TENG array and five synapse transistors are integrated to handle and process multiple inputs. And three encoding strategies based on activity-dependent spiking form the alphabet code directories. Further implementation of neural encoding, learning, and memory in such an integrated neuromorphic system is expected to provide a promising way for biomimetic tactile sensation, human–machine interfaces, and artificial neural network algorithms.

4 | MATERIALS AND METHODS

4.1 | Fabrication of functional materials

4.1.1 | Preparation of stretchable PEDOT:PSS

PEDOT:PSS were synthesized by mixing 10 mL of aqueous dispersion (Clevios PH1000) with 5 vol% ethylene glycols to improve film conductivity, 0.25 vol% 4-dodecylbenzenesulfonic acid (DBSA) to enhance film homogeneity, and 1 vol% crosslinker of (3-glycidyloxypropyl) trimethoxysilane, as our previous work reported.[24] Then stir the mixed solution for 2 days at room temperature. To make PEDOT:PSS stretchable, a soft polymer of poly(2-acrylamido-2methyl-1-propanesulfonic acid) (PAAMPSA, average M_w of 2 000 000, 15 wt% in H_2O, Sigma-Aldrich) was added into the prepared PEDOT:PSS solution with a ratio of 30 wt% and followed by stirring for 1 h.

4.1.2 | Preparation of stretchable hydrogel

First, dissolving NaCl (0.5 M, Sigma-Aldrich), acrylamide (AAm, 1.75 M, Sigma-Aldrich), polyacrylamide (0.142 wt % of AAm) in deionized water and stirring the mixed solution at 60°C for 4 h until the materials dissolved completely. Then, adding crosslinker N',N-methylenebisacrlamide (1 wt% of AAm) and the photoinitiator of Irgacure 1173 (1.6 wt% of AAm) to the mixed solution and stir for 2 h. Pouring the prepared ionic hydrogel into the plastic mold with a thickness of 100 μm and exposing them under a UV lamp for 15 min. Cutting the cured hydrogel by laser cutting machine into

2 cm × 1 cm. Peeling off the hydrogel patches and attaching them onto the regions of gate electrodes and PEDOT:PSS channels.

4.2 | Fabrication of stretchable neuromorphic tactile system

The schematic illustration of the fabrication process is shown in Figure S1. First, wipe hand sanitizer on clean glass slides blasted with plasma gas, then bake slides at 100°C for 1 min. PDMS elastomer and cross-linker were mixed in a ratio of 30:1 wt%, after adding commercial dyes, then the mixture was degassed with a pump to get rid of bubbles. Then PDMS was spin-coated on the glass slides with a speed of 300 rpm, and baked at 80°C for 4 h, with a thickness of ∼500 μm to ensure tissue-compatible flexibility and easy peeling from glass slides. A 10-min UV-Ozone treatment is used to enhance the hydrophilicity of PDMS surface. The TENG bottom electrode, biomimetic nerve fibers, and source-drain-gate electrodes were formed by blade coating liquid metal of Eutectic Gallium-Indium (EGaIn, Ga = 75.5%, In = 24.5%, Sigma-Aldrich) with the aid of PET masks. These PET masks are engraved via a laser engraving machine (3020, WANHAO LASER Company). In Figure S2, electrode patterns on PDMS laminated with two input terminals integrated with one synapse transistor, and 25 input terminals integrated with five synapse transistors are displayed. And Figure S3 displays their skin-conformable and seamless lamination capabilities. Then laminating PDMS friction layer (10:1) with the size of 8 × 8 mm² onto the EGaIn electrodes. Followed by spray coating prepared PEDOT:PSS (∼10 μm) on channel region with a size of 300 × 50 μm², and then baked at 80°C for 2 h. Next, fix the hydrogel patches (with the thickness of 200 μm) onto the surfaces of gate electrode and PEDOT:PSS. After encapsulating the device with PDMS (30:1), then peel off the devices from the glass substrates. Finally, fixing prepared PDMS (30:1, 500 μm)/liquid metal (25 μm)/PDMS (20:1, 100 μm, the second friction layer) on a volunteer's finger to conduct experiments (Figure S4).

4.3 | Device characterization

The sheet resistances of EGaIn electrodes were measured by a four-probe tester (DMR-10). Normalized resistance of hydrogel and PEDOT:PSS were measured by multimeter. The output currents of TENG were obtained by a low-noise current preamplifier (Model SR570, Stanford Research System) with computer measurement software written in LabVIEW. The output voltages of TENG were measured with a Digital Storage Oscilloscope (DSOX2014A, KYSIGHT). Electrochemical performance of OECT, tactile sensing demonstrations were characterized by a semiconductor analyzer (Keysight B1500A). The thickness was measured by the Bruker Dektak XT Profilometer and caliper (DUAK CA2, measurement accuracy of 10 μm). The tensile tests of PEDOT:PSS and hydrogel electrolyte were conducted by an Instron 5942 Micro Newton Tester. During the test, PEDOT:PSS was laminated onto the PDMS substrate (30:1), while hydrogel electrolyte was a free-standing film.

4.4 | Calculation

4.4.1 | Pressure sensitivity

Pressure sensitivity is defined as $S = (\Delta V/V_{max})/\Delta P$, where ΔV is the difference between V_{OC} and V_0, V_{max} is the maximum value of V_{OC}, and ΔP is the change in applied pressure.

4.4.2 | Energy consumption

The energy consumption of synapse transistor is the sum of resistive-related energy ($E_{resistive}$) and capacitive-related energy ($E_{capacitive}$). $E_{resistive}$ is defined as $I_{ds} \times V_{ds} \times t_{duration}$, where I_{ds} and V_{ds} refer to the peak current of the postsynaptic current and the drain voltage, and the $t_{duration}$ refers to the pulse maintenance time. $E_{capacitive}$ is evaluated by the equation $E_{capacitive} = C_{eff} \times V_{ps}^2/2$, where C_{eff} and V_{ps} are the effective capacitance and the externally supplied presynaptic spike voltage, respectively. In self-powered synapse transistor, the $E_{capacitive}$ is replaced by the mechanical energy of TENG, without any electric energy consumption, which means V_{ps} is 0. Consequently, the total energy consumption depends only on $E_{resistive}$.

4.4.3 | Curve fitting

In Figure 1G, the responses of TENG output to pressure and frequency are fitted as a linear relationship for differences.

4.4.4 | Error bar

To obtain more general and convincing results, all experiments were conducted more than six times. And the standard deviations, which present the dispersion level, are displayed in the form of the error bar in data figures. The

standard deviation is defined as $S = \sqrt{\frac{\sum_{i=1}^{n}(x_i - \overline{x})}{n-1}}$, where x_i and $\overline{x}$ refer to the raw data and their average value, respectively. Therefore, data in Figures 1D,G, 2E,G,H,L, and 3D,F were displayed in the form of average value ± standard deviation (error bar).

CONFLICT OF INTEREST STATEMENT
The authors declare no conflict of interest.

ORCID
Zijian Zheng https://orcid.org/0000-0002-6653-7594
Xinge Yu https://orcid.org/0000-0003-0522-1171

REFERENCES

1. Pulvermüller F, Tomasello R, Henningsen-Schomers MR, Wennekers T. Biological constraints on neural network models of cognitive function. *Nat Rev Neurosci.* 2021;22(8):488-502.
2. Lee DH, Park GH, Kim SH, et al. Neuromorphic devices based on fluorite-structured ferroelectrics. *InfoMat.* 2022;4(12):e12380.
3. Woo S-H, Lumpkin EA, Patapoutian A. Merkel cells and neurons keep in touch. *Trends Cell Biol.* 2015;25(2):74-81.
4. Yu J, Wang Y, Qin S, et al. Bioinspired interactive neuromorphic devices. *Mater Today.* 2022;60:158-182.
5. Chun S, Kim J-S, Yoo Y, et al. An artificial neural tactile sensing system. *Nat Electron.* 2021;4(6):429-438.
6. Chen Y, Gao G, Zhao J, et al. Piezotronic graphene artificial sensory synapse. *Adv Funct Mater.* 2019;29(41):1900959.
7. Wang WS, Zhu LQ. Recent advances in neuromorphic transistors for artificial perception applications: focus issue review. *Sci Technol Adv Mater.* 2023;24(1):10-41.
8. Kwon OS, Song HS, Park SJ, et al. An ultrasensitive, selective, multiplexed superbioelectronic nose that mimics the human sense of smell. *Nano Lett.* 2015;15(10):6559-6567.
9. Tan H, Tao Q, Pande I, et al. Tactile sensory coding and learning with bio-inspired optoelectronic spiking afferent nerves. *Nat Commun.* 2020;11(1):1369.
10. Dai S, Wu X, Liu D, et al. Light-stimulated synaptic devices utilizing interfacial effect of organic field-effect transistors. *ACS Appl Mater Interfaces.* 2018;10(25):21472-21480.
11. Guo H, Pu X, Chen J, et al. A highly sensitive, self-powered triboelectric auditory sensor for social robotics and hearing aids. *Sci Robot.* 2018;3(20):eaat2516.
12. Liu Y, Li E, Wang X, et al. Self-powered artificial auditory pathway for intelligent neuromorphic computing and sound detection. *Nano Energy.* 2020;78:105403.
13. Shastri BJ, Tait AN, Ferreira de Lima T, et al. Photonics for artificial intelligence and neuromorphic computing. *Nat Photonics.* 2021;15(2):102-114.
14. Kim JP, Kim SK, Park S, et al. Dielectric-engineered high-speed, low-power, highly reliable charge trap flash-based synaptic device for neuromorphic computing beyond inference. *Nano Lett.* 2023;23(2):451-461.
15. Lee YR, Trung TQ, Hwang B-U, Lee NE. A flexible artificial intrinsic-synaptic tactile sensory organ. *Nat Commun.* 2020;11(1):2753.
16. Kim Y, Chortos A, Xu W, et al. A bioinspired flexible organic artificial afferent nerve. *Science.* 2018;360(6392):998-1003.
17. Zhao LM, Li H, Meng JP, Li Z. The recent advances in self-powered medical information sensors. *InfoMat.* 2020;2(1):212-234.
18. Zhang C, Li S, He Y, et al. Oxide synaptic transistors coupled with triboelectric nanogenerators for bio-inspired tactile sensing application. *IEEE Electron Device Lett.* 2020;41(4):617-620.
19. Shao L, Zhao Y, Liu Y. Organic synaptic transistors: the evolutionary path from memory cells to the application of artificial neural networks. *Adv Funct Mater.* 2021;31(28):2101951.
20. Xu W, Min S-Y, Hwang H, Lee TW. Organic core-sheath nanowire artificial synapses with femtojoule energy consumption. *Sci Adv.* 2016;2(6):e1501326.
21. Wang YA, Zheng Y, Gao J, et al. Band-tailored van der Waals heterostructure for multilevel memory and artificial synapse. *InfoMat.* 2021;3(8):917-928.
22. Yang L, Wang Z, Zhang S, et al. Neuromorphic gustatory system with salt-taste perception, information processing, and excessive-intake warning capabilities. *Nano Lett.* 2022;23(1):8-16.
23. Yu J, Gao G, Huang J, et al. Contact-electrification-activated artificial afferents at femtojoule energy. *Nat Commun.* 2021;12(1):1581.
24. Wu M, Yao K, Huang N, et al. Ultrathin, soft, bioresorbable organic electrochemical transistors for transient spatiotemporal mapping of brain activity. *Adv Sci.* 2023;10(14):2300504.
25. Peng Y, Gao L, Liu C, et al. Stretchable organic electrochemical transistors via three-dimensional porous elastic semiconducting films for artificial synaptic applications. *Nano Res.* 2023;16(7):10206-10214.
26. Fuard D, Tzvetkova-Chevolleau T, Decossas S, Tracqui P, Schiavone P. Optimization of poly-di-methyl-siloxane (PDMS) substrates for studying cellular adhesion and motility. *Microelectron Eng.* 2008;85(5-6):1289-1293.
27. Park S, Yoon HJ. New approach for large-area thermoelectric junctions with a liquid eutectic gallium-indium electrode. *Nano Lett.* 2018;18(12):7715-7718.

28. Yao K, Liu Y, Li D, et al. Mechanics designs-performance relationships in epidermal triboelectric nanogenerators. *Nano Energy*. 2020;76:105017.

29. Guan X, Xu B, Huang J, Jing T, Gao Y. Fiber-shaped stretchable triboelectric nanogenerator with a novel synergistic structure of opposite poisson's ratios. *Chem Eng J*. 2022;427:131698.

30. Li W, Pei Y, Zhang C, Kottapalli AGP. Bioinspired designs and biomimetic applications of triboelectric nanogenerators. *Nano Energy*. 2021;84:105865.

31. Chun S, Hwang I, Son W, Chang JH, Park W. Recognition, classification, and prediction of the tactile sense. *Nanoscale*. 2018;10(22):10545-10553.

32. Chortos A, Liu J, Bao Z. Pursuing prosthetic electronic skin. *Nat Mater*. 2016;15(9):937-950.

33. Han S, Yamamoto S, Polyravas AG, Malliaras GG. Microfabricated ion-selective transistors with fast and supernernstian response. *Adv Mater*. 2020;32(48):2004790.

34. Rivnay J, Inal S, Salleo A, Owens RM, Berggren M, Malliaras GG. Organic electrochemical transistors. *Nat Rev Mater*. 2018;3(2):1-14.

35. Su X, Wu X, Chen S, et al. A highly conducting polymer for self-healable, printable, and stretchable organic electrochemical transistor arrays and near hysteresis-free soft tactile sensors. *Adv Mater*. 2022;34(19):2200682.

36. Ge Q, Chen Z, Cheng J, et al. 3D printing of highly stretchable hydrogel with diverse uv curable polymers. *Sci Adv*. 2021;7(2): eaba4261.

37. Zeng J, Zhao J, Bu T, et al. A flexible tribotronic artificial synapse with bioinspired neurosensory behavior. *Nanomicro Lett*. 2023;15(1):1-15.

38. Kaphle V, Liu S, Keum CM, Lüssem B. Organic electrochemical transistors based on room temperature ionic liquids: performance and stability. *Phys Status Solidi A*. 2018;215(24): 1800631.

39. Giridharagopal R, Flagg L, Harrison J, et al. Electrochemical strain microscopy probes morphology-induced variations in ion uptake and performance in organic electrochemical transistors. *Nat Mater*. 2017;16(7):737-742.

40. Huang W, Chen J, Yao Y, et al. Vertical organic electrochemical transistors for complementary circuits. *Nature*. 2023; 613(7944):496-502.

41. Xie M, Liu H, Wu M, et al. Cycling stability of organic electrochemical transistors. *Org Electron*. 2023;117:106777.

42. Dai S, Dai Y, Zhao Z, et al. Intrinsically stretchable neuromorphic devices for on-body processing of health data with artificial intelligence. *Matter*. 2022;5(10):3375-3390.

43. Chen J, Huang W, Zheng D, et al. Highly stretchable organic electrochemical transistors with strain-resistant performance. *Nat Mater*. 2022;21(5):564-571.

44. Wu X, Surendran A, Ko J, et al. Ionic-liquid doping enables high transconductance, fast response time, and high ion sensitivity in organic electrochemical transistors. *Adv Mater*. 2019;31(2):1805544.

45. Zeglio E, Inganäs O. Active materials for organic electrochemical transistors. *Adv Mater*. 2018;30(44):1800941.

46. Khodagholy D, Rivnay J, Sessolo M, et al. High transconductance organic electrochemical transistors. *Nat Commun*. 2013;4(1):2133.

47. Fairhall AL, Lewen GD, Bialek W, De Ruyter Van Stevenick RR. Efficiency and ambiguity in an adaptive neural code. *Nature*. 2001;412(6849):787-792.

48. Gkoupidenis P, Schaefer N, Garlan B, Malliaras GG. Neuromorphic functions in PEDOT: PSS organic electrochemical transistors. *Adv Mater*. 2015;27(44):7176-7180.

SUPPORTING INFORMATION

Additional supporting information can be found online in the Supporting Information section at the end of this article.